Volume 1 | Number 1 | Jan 2013 | Pages 1–100

Journal of
Materials Chemistry B

Materials for biology and medicine
www.rsc.org/materialsB

ROYAL SOCIETY OF CHEMISTRY

ROYAL SOCIETY OF CHEMISTRY

www.rsc.org/materialsB

Journal of Materials Chemistry B

ARTICLE

Metal chelate grafting at the surface of mesoporous silica nanoparticles (MSNs): physico-chemical and biomedical imaging assessment

Myriam Laprise-Pelletier,[a,b,d] Meryem Bouchoucha,[a,c,d] Jean Lagueux,[a] Pascale Chevallier,[a,d] Roger Lecomte,[e] Yves Gossuin,[f] Freddy Kleitz,[c,d,*] and Marc-André Fortin[a,b,d,*]

Mesoporous silica nanoparticles (MSNs) are being developed as drug delivery vectors. Biomedical imaging (MRI and PET) enables their tracking *in vivo*, provided their surface is adequately grafted with imaging probes (metal chelates). However, MSNs are characterized by huge specific surfaces, and high-quality metal chelate anchoring procedures must be developed and validated, to demonstrate that their detection *in vivo*, is associated to the presence of nanoparticles and not to detached metal chelates. MCM-48 nanospheres (M48SNs, 150 nm diam., 3-D pore geometry) were synthesized and functionalized with diethylenetriaminepentaacetic acid (DTPA). The strong grafting of DTPA was confirmed by ^{29}Si NMR, XPS, FTIR and TGA. The particles were labeled with paramagnetic ions Gd^{3+} (for MRI) as well as radioactive ions $^{64}Cu^{2+}$ (for PET; half-life: 12.7 h). Gd^{3+}-DTPA-M48SNs formed a stable colloid in saline media for at least 6 months, without any sign of aggregation. The relaxometric properties were measured at various magnetic fields. The strength of DTPA binding at the surface of MSNs was also assessed *in vivo*, by injecting mice (i.v.) with $Gd^{3+}/^{64}Cu^{2+}$-DTPA-M48SNs. Vascular retention and urinary clearance were monitored by MRI, whereas the PET modality provided dynamic and quantitative assessment of biodistribution and blood/organ clearance. No significant ^{64}Cu activity was detectable in the bladder. The study confirmed the very limited detachment of DTPA from M48SNs cores once injected *in vivo*. The transit of MSN through the liver and intestinal tract, does not lead to evidences of $Gd^{3+}/^{64}Cu^{2+}$-DTPA in the urine. This physico-chemical and biodistribution study confirms the quality of DTPA attachment at the surface of the particles, necessary to allow further development of PET/MRI-assisted MSN-vectorized drug delivery procedures.

Introduction

Mesoporous silica nanoparticles (MSNs), a new class of nanostructured materials, have considerable potential as drug delivery vectors and for other theranostic biomedical applications.[1-15] Their size (20 - 200 nm mean diam.), high pore volume (0.6 – 1 cm^3/g), surface chemistry and functional coatings can be precisely tuned and adapted to different applications. In general, drug loadings higher than 30% wt can be achieved in these nanoconstructs and MSNs can serve as delivery carriers for controlled drug and gene release.[16-24] The first silica-based diagnostic nanoparticles are now entering the clinical stage.[1, 25] Compared to their organic or polymer counterparts, drug delivery vectors based on inorganic porous materials could provide extended mechanical strength, chemical stability, biocompatibility and resistance to microbial attack.[4] The versatility of MSNs physico-chemical surface functionalization could provide a second life to a number of drugs that have not made it to the clinic due either to poor solubility, poor targeted delivery to

organs, or to the occurrence of extensive side effects.[5] Indeed, the long-term goal of MSN-based formulations is the development of vehicles that could more efficiently deliver drugs to specific organs or cells, while decreasing the side effects of medication.

In order to do so, it is necessary to label MSNs with imaging probes, enabling their detection *in vivo* using either magnetic resonance imaging (MRI), positron emission tomography (PET), or a combination of both modalities (PET/MRI).[26] Metal chelates (e.g. Gd^{3+} for MRI, and $^{64}Cu^{2+}$ for PET) grafted at the surface of the particle, allow the monitoring of MSN-vectorized drug delivery to organs. In particular, several studies have reported on the development of MSNs labeled with paramagnetic Gd-based chelates, which appear bright in T_1-weighted MR imaging. Such products are mostly based on the grafting of Gd(III) chelates (e.g.,DTPA, diethylenetriaminepentaacetic acid) at the surface of MSNs.[27-30] However, this class of materials is characterized by huge specific surfaces (500 – 1500 m^2/g). Therefore, the quality and strength of

metal chelate grafting at the surface of the particles must be demonstrated to unambiguously validate that signal enhancement (in MRI) or activity counting (in PET) comes from the nanoparticles and not from metal chelates detaching from the main MSN cores. At this stage of their development, many unknowns remain on the chemical stability of metal chelate grafting at MSNs, once injected *in vivo*, and such procedures must be validated with both *in vitro* physico-chemical techniques, as well as *in vivo* through adequate imaging procedures.

In vivo magnetic resonance imaging (MRI) and positron emission tomography (PET) enable the visualization of nanoparticle biodistribution in real-time and on the same animal over long periods. Whereas MRI, as high-resolution, whole-body anatomical imaging technique, is suitable to monitor the blood retention and urine excretion of MSN labeled with paramagnetic elements [30], it does not always provide very clear evidence of moderate MSN uptake and retention in critical organs such as liver, spleen, and kidneys. To perform quantitative, whole-body, and dynamic pharmacokinetic profiles of MSN injected *in vivo*, PET is much more appropriate as it allows the detection of imaging tracers in the nanomolar range. Until now, no quantitative biodistribution study has been reported using the unique combination of PET/MRI imaging modalities, enabling the dynamic acquisition of MSN uptake to key organs. More specifically, dynamic PET biodistribution studies would reveal the biodistribution of MSN in the first minutes following intravenous (i.v.) injections (kinetics of liver and spleen uptake; blood clearance; evidences of kidney excretion). Finally, evidences of free DTPA in the blood, would be efficiently revealed thereby (e.g. through evidences of rapid kidney and bladder clearance). Indeed, nanoparticles of the size of MSNs (> 25 nm diam.) are not expected to follow the urinary clearance route.

Until now, most experiments reporting on the development of MSN for biomedical applications have been performed *in vitro*, with very few results available of systematic biodistribution studies *in vivo*. None of these studies have reported blood clearance and organ uptake profiles quantitatively, and at high temporal resolution, and none have shown a clear demonstration of the fraction of metal chelates eventually detaching from the MSN cores. In addition to this, the variety of study designs and lack of standardization makes the comparison between MSNs from different research groups a difficult task.

A comprehensive description of MSN synthesis procedures can be found in previous literature.[4] In general, TEOS-CTAB-amphiphilic block copolymer-based MSN synthesis lead to materials with mesopore diameters in the range 3-4 nm, ordered in either 2-D or 3-D arrangements, and with porosity higher than 50% v/v. In this study, MCM-48 nanospheres (150 nm diam., 3-D) were synthesized and functionalized with diethylenetriaminepentaacetic acid (DTPA) through intermediate reaction with aminopropyltriethoxysilane (APTES). Silane coupling efficiency was measured by ^{29}Si NMR. The strong grafting of DTPA chelates was confirmed by XPS, FTIR and TGA, before and after chelation with Gd^{3+}. Gd^{3+}-DTPA-M48SNs formed a stable colloid in saline media for at least 6 months, without any sign of aggregation. The relaxometric properties were measured at various magnetic field strengths, to reveal a profile that correspond closely to that of other paramagnetic nanoparticles or macromolecules (and not of free Gd^{3+}-DTPA). Finally, DTPA binding at the surface of the particles was assessed *in vivo*. For this, mice were injected (i.v.) with Gd^{3+}/Cu^{2+}-DTPA-M48SNs. The vascular

retention and urine clearance were both monitored by MRI, whereas the PET modality provided a comprehensive, dynamic and quantitative assessment of biodistribution and blood/organ clearance.

Experimental

Materials and methods

Synthesis of DTPA-grafted mesoporous silica nanoparticles (M48SNs). Unless specified, all chemical products used in this study were from Sigma-Aldrich (Oakville, Ontario, Canada) without any further purification. MCM-48 nanospheres (M48SNs) with a 3-D $Ia\bar{3}d$ cubic network of pores were synthesized by adapting a previously reported procedure.[31] In brief, 1.0 g of n-cetyltrimethylammonium bromide (CTAB, 99%) and 4.0 g of Pluronic F127 ($EO_{106}PO_{70}EO_{106}$, BioReagent) were dissolved in 298 mL of H_2O/NH_3/EtOH (NH$_4$OH(aq) (2.8 wt %)/EtOH = 2.5/1 (v/v)) under vigorous stirring. Then, 3.6 g of tetraethylorthosilicate (TEOS, 98%) was added to the solution and vigorously stirred for 1 minute at room temperature (RT). The reaction mixture was kept 24 h in static conditions (air, RT) and the resulting white solid product was isolated by centrifugation at 15 300 g for 25 min, rinsed once with water (250 mL) and twice with ethanol (250 mL), then dried overnight (air, 70 °C). Then, M48SNs (1 g) were refluxed in toluene (100 mL) for 24 h with 1.9 mL of aminopropyltriethoxysilane (APTES). The particles were recovered by centrifugation and washed three times with ethanol (50 mL). Because the particles are synthesized by using n-cetyltrimethylammonium bromide (CTAB) and Pluronic F127 ($EO_{106}PO_{70}EO_{106}$, BioReagent) to form the template, a solvent extraction step was performed by refluxing the particles for 24 h in ethanol (1 g M48SNs/100 mL ethanol 95%) supplemented with 1% v/v HCl (37%). The particles were collected by centrifugation, washed twice in 20 mL of ethanol (95%), and undispersed particles, eliminated by centrifugation (500 g, 10 min). These aminated particles were dried overnight (air, 70 °C), and are referred to as "APTES-M48SNs".

DTPA grafting on M48SNs. APTES-M48SNs nanoparticles (100 mg) were dispersed in dry DMSO, followed by addition of diethylenetriaminepentaacetic acid (DTPA) bis-anhydride (> 98.5%) in a APTES-M48SNs:DTPA massic ratio of 2:1. This solution was stirred overnight. The particles ("DTPA-M48SNs") were isolated by centrifugation (7500 g, 10 min), washed three times with DMSO, resuspended in 10 mL of DMSO and stored until labeling with Gd^{3+} and $^{64}Cu^{2+}$ (referred to as "$Gd^{3+}/^{64}Cu^{2+}$-DTPA-M48SNs"). The metal chelate grafting procedure is comprehensively described in the schematic representation of Fig. 1.

M48SNs and DTPA-M48SNs textural properties. The porosity features and textural properties of M48SNs and DTPA-M48SNs were measured by X-ray diffraction at low angles as well as by nitrogen physisorption. The massic fraction of DTPA grafted on M48SNs, was measured by thermogravimetric analysis (TGA) (detailed in the ESI, Fig. S1-S4).

Nanoparticle size analysis with TEM. The mean particle size diameter of DTPA-M48SNs was measured using particles deposited on a carbon-coated copper grid, and imaged in TEM (Jeol JEM-1230, 80 keV, Tokyo, Japan), followed by calculations through a ImageJ protocol (sample of 1495 particles, from 5 images taken over 5 different quartiles). The results are shown in Fig. 1A. High-resolution images were acquired on a Jeol JEM-2100F, 200 keV (Fig. 1B).
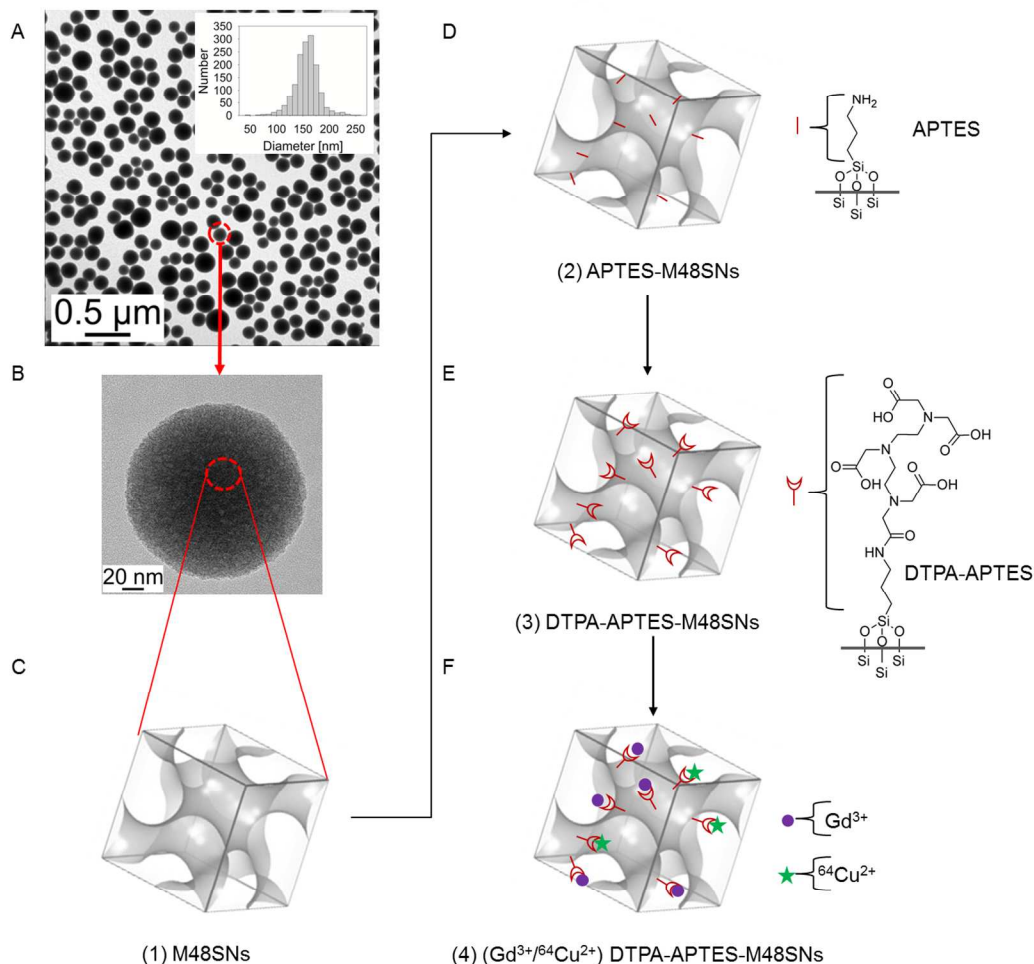
Fig. 1 M48SN synthesized as drug carriers were visualised by TEM (**A-B**). In (**C**), schematic representation of the $Ia\bar{3}d$ pore network, followed by grafting of APTES (**D**), DTPA (**E**), and labelling with $Gd^{3+}/^{64}Cu^{2+}$ (**F**).

Labeling and purification of M48SNs with Gd^{3+}. 1.5 mL of DTPA-M48SNs (in DMSO, 3.6 M Si) was washed three times with nanopure water, using centrifugation cycles (1.5:4.5 v/v, 4300 g, 15 min). The supernatant was discarded, and one (1) mL of a 100 mM-solution of $Gd(CH_3CO_2)_3 \cdot xH_2O$ was added dropwise to DTPA-M48SNs particles. The solution was left for chelation (30 min, RT, moderate agitation). Then, the particles were eluted on a chromatography column (model XK 26/40, Pharmacia, Uppsala, Sweden) filled with Sephadex G-25 (coarse, 28 cm, GE Healthcare Bio-Sciences AB, Uppsala, Sweden). Since the radioisotope $^{64}Cu^{2+}$ has a half-life of 12.7 hours, matching the requirements for biodistribution kinetics of MSNs *in vivo*, it is necessary to minimize the complexation time, as well as to develop fast and reliable purification procedures to remove all free metal ions from the nanoparticle suspension, before injection. The particles were eluted with 154 mM NaCl (0.22 μm-filtered), as the buffer for equilibration and elution at a constant flow rate (5 mL/min; peristaltic pump). The void (first 48 mL) was discarded, and the labeled M48SNs were collected in the next 25 mL fraction. Tangential filtration (10 kD, 11 cm², polysulfone, MicroKros, Spectrum Laboratories, Rancho Dominguez, CA, USA) was used to concentrate the nanoparticles suspension up to ^1H longitudinal relaxation times (T_1) values < 30 ms. Altogether, the purification steps (chromatography and

concentration) were performed in not more than 60 min. This nanoparticle suspension was referred to as Gd^{3+}-DTPA-M48SNs.

M48SNs, APTES-M48SNs, DTPA-M48SNs, and Gd^{3+}-DTPA-M48SNs physico-chemical characterisation

NMR. Solid-state magic-angle spinning (MAS) nuclear magnetic resonance (NMR) spectra were obtained on a Bruker DRX300 MHz NMR spectrometer. The 59.60 MHz ^{29}Si MAS NMR and the 75.4 MHz ^{13}C CP-MAS NMR spectra were measured using 4 mm rotors spinning at 8 kHz. The chemical shifts are reported in ppm relative to tetramethylsilane (TMS) for ^{29}Si and relative to Adamantane for ^{13}C. The results are shown in Fig. 2A, B.

EDX. The Gd/Si ratio in Gd^{3+}-DTPA-M48SNs suspension, was measured with energy dispersive X-ray spectroscopy (EDX) analyses, performed with a high resolution TEM (Jeol JEM-2100F, 200 keV).

XPS. The chemical composition of nanoparticles and complexation of Gd^{3+} in DTPA was investigated by X-ray photoelectron spectroscopy (XPS). For XPS analyses, drops (20 μL) of aqueous suspensions of nanoparticles were deposited on gold-coated silicon substrates cleaned with TL1 solution, which is a mixture of ultrapure

water, 30% H_2O_2 and 25% ammonia (Fisher, IL, USA; 5:1:1), at 80 °C for 10 min. The drops were dried in a vacuum oven (at 40 °C). The samples were then analyzed by using a PHI 5600-ci spectrometer (Physical Electronics, Eden Prairie, MN, USA). An achromatic aluminum X-ray source (1486.6 eV, 200 W) was used to record the survey spectra (1400-0 eV) with charge neutralization while high resolution spectra (HRXPS) were obtained using an achromatic magnesium X-ray source (1253.6 eV, 150 W) with no charge compensation. The detection angle was set at 45° with respect to the surface and the analyzed area was 0.005 cm^2. The curve fitting procedure of the components underlying the C1s peaks was performed by means of a least-square minimization procedure employing Gaussian–Lorentzian functions and a Shirley-type background.

FTIR. Further investigations on chemical structure of the nanoparticles suspension were done with attenuated Total Reflectance-Fourier Transform Infrared spectroscopy (ATR-FTIR). These analyses were performed using a Nicolet Magna 550 Fourier transform infrared spectrometer (Thermo Nicolet, Madison, WI, USA) equipped with a germanium-coated KBr beamsplitter and a DTGS/KBr detector. Samples (20 µL) of the aqueous suspensions of nanoparticles were directly deposited on the Si crystal and then dried under vacuum at 40 °C. Spectra were recorded in absorbance mode and 100 scans were recorded with a spectral resolution of 4 cm^{-1}. A Gd-DTPA solution was prepared as reference to compare with the Gd^{3+}-DTPA-M48SNs spectra. For this, 5 mM of $Gd(CH_3CO_2)_3 \cdot xH_2O$ was complexed with 5 mM of DTPA in aqueous solution.

Hydrodynamic diameter and zeta potential of (Gd^{3+})-DTPA-M48SNs. The hydrodynamic diameter of particles in saline, was measured by dynamic light scattering (DLS; He-Ne laser (633 nm); scattering angle = 173 °; T = 25 °C; Nano zetasizer, Malvern Instruments Ltd., UK). The viscosity of water was fixed at 0.8872 cP and refractive index of water and silica were fixed at 1.33 and 1.45, respectively. The results were calculated from the average of three measurements. For colloidal stability assessment, a sample was left at room temperature for 6 months, and measured. Zeta potential of Gd^{3+}-DTPA-M48SNs was measured by electrophoretic light scattering (ELS; He-Ne laser (633 nm); scattering angle = 173 °; T = 25 °C; at pH = 7.5. The result was calculated from the average of three measurements.

Relaxometric studies of Gd^{3+}-DTPA-M48SNs. Aliquots of diluted Gd^{3+}-DTPA-M48SNs suspension (300 µL; 100, 75, 50, 25% v/v) were distributed in 7 mm o.d. NMR tubes. The relaxation times (T_1 and T_2) were measured with a TD-NMR relaxometer (Minispec 60 mq, 60 MHz (1.41 T), 37°C, Bruker, Billerica, MA, USA). Then, longitudinal and transverse relaxation rates ($1/T_1$, $1/T_2$) were plotted against Gd concentrations, and relaxivities (r_1 and r_2) were calculated from the slope of the graphs. For this, Gd concentration values were obtained by ICP-MS (PerkinElmer Elan 6000, Waltham, MA, USA), after digestion of samples in nitric acid (trace metal grade, Fisher) and 30 % H_2O_2 at high temperature (115 °C). Nuclear magnetic relaxation dispersion (NMRD) profiles (T_1) of aqueous suspensions were measured from 0.015 to 40 MHz with a Spinmaster fast field cycling relaxometer (STELAR, Mede, Italy) at 37 °C, using 600 µL of the 100% v/v nanoparticles suspension. Then, longitudinal and transverse relaxation times (T_1 and T_2) were measured at 20, 60, 300 and 500 MHz (corresponding to 0.47, 1.41, 7.0 and 11.7 T; 1 T = 42.6 MHz) by using Bruker MiniSpec relaxometers (20 and 60 mq; 20 and 60 MHz), and Bruker AMX300 (300 MHz) and AVANCEII-500 spectrometers (500 MHz). The temperature was set to 37 °C for all measurements, as well as a standard echo time of 1 ms. Finally,

the relaxation rates ($1/T_1$ and $1/T_2$) were normalized to the Gd^{3+} concentration values in order to calculate the relaxivities (r_1 and r_2).

***In vivo* MR imaging and signal enhancement studies (Gd^{3+}-DTPA-M48SNs)**

All animal experiments were conducted under the guidelines of Université Laval, Université de Sherbrooke and Centre hospitalier universitaire de Québec (CHU de Quebec, Canada) animal ethical committee. Six week-old balb/c female mice (Charles River, Montreal, Canada), were anaesthetised with isoflurane using a nose cone integrated to the MRI mouse bed. Animals were cannulated in the caudal tail vein (30 G, winged needle), and connected to a catheter prewashed with heparin and connected to the contrast media syringe (280 µm ID Intramedic™ Polyethylene Tubing PE-10, 60 cm, total volume: 60 µL). Then, the animals were inserted in a 3.5 cm diameter RF coil, and scanned twice using a T_1-weighted 2D spin echo sequence (FOV: 90 mm, 24 slices, 0.7 mm, 0.1 slice gap, dwell time 25 µs, 400x320, fα 90°, TE/TR: 18/800 ms, duration: 4:16 min). Respiratory triggering was used. At time t = 0, the animals (3) were injected with 100 µL of nanoparticle suspension (Gd^{3+}-DTPA-M48SNs in 154 mM NaCl, T_1 = 19.4 ms, ~ 2 mM Gd), and the same MR sequence was repeated for at least 90 minutes. For signal analysis, raw signal data were extracted, and regions of interest (ROIs) drawn over sections of the abdominal aorta, liver and bladder. The mean signal intensity was calculated using ImageJ software (version 1.44m; Wayne Rasband, National Institutes of Health, Bethesda, MD, USA). Signal enhancement ratios were calculated as follows:

$$Ratio_{t=x} = \frac{Signal_{t=x}}{Signal_{t=0}}$$ Equation 1

PET and biodistribution studies

The radioisotope $^{64}Cu^{2+}$ ($t_{1/2}$ = 12.7 h) was purchased from the Sherbrooke Molecular Imaging Center of CRCHUS (Quebec, Canada), in the form of copper acetate ($^{64}Cu^{2+}(CH_3CO_2)_2$). The preparation of copper acetate is described in the Supporting information section.

Labeling with $^{64}Cu^{2+}$ and Gd^{3+} ($Gd^{3+}/^{64}Cu^{2+}$-DTPA-M48SNs). A fraction (500 µL) of the $^{64}Cu^{2+}$ solution (8.36 mCi) was added to the stock DTPA-M48SNs suspension (1.5 mL of 3.6 M Si) and left for chelation under moderate stirring (90 min, RT). After complexation with $^{64}Cu^{2+}$, 500 µL of a solution of $Gd(CH_3CO_2)_3 \cdot xH_2O$ (100 mM) was added, and the nanoparticle suspension was left in incubation for 30 min (RT). The suspension was purified by SEC (in 154 mM NaCl) and concentrated by tangential filtration down to 1.5 mL (see aforementioned procedure) in less than 60 minutes. From the SEC results, the radioactive labeling yield was evaluated to (54%). Similar T_1 and T_2 results were obtained with $^{64}Cu^{2+}$ and Gd^{3+}, compared to Gd^{3+} only.

Biodistribution studies. PET imaging was performed using a LabPET8 scanner (Gamma Medica, Northridge, CA, USA) with an 8-cm axial field, achieving a high spatial resolution (<1.5 mm FWHM within the central 12-mm diameter field of view) and absolute sensitivity (2.6% at an energy threshold of 250 keV).[32] Four week-old balb/c female mice (n = 4, Charles River, Montreal, Canada), were anaesthetized with isoflurane using a nose cone integrated to the PET mouse bed. Animals were cannulated in the caudal tail vein (30 G, winged needle), and connected to a catheter prewashed with heparin and connected to the syringe (280 µm ID Intramedic™ Polyethylene Tubing PE-10, 60 cm, total volume: 6

μL). The first animal was injected 17 h after beginning of chelation with $^{64}Cu^{2+}$ (~100 μCi at t = 0) and the others subsequently for the scans. Each animal was injected with 100-150 μL of $Gd^{3+}/^{64}Cu^{2+}$-DTPA-M48SNs. The total activity injected per animal amounted 170 (100 μL), 213, 210 and 180 (150 μL) μCi for each mouse, respectively. Dynamic scans were acquired for 60 min, followed by static whole-body scans at t = 6, 12, 24 and 48 h. A 30-min acquisition scan was performed at t = 6 h, then 60-min scans at t = 12 h, 24 h and 48 h. At the end of each acquisition, data were reconstructed and corrected for radioactivity decay. In the following analysis, doses were corrected for radioactive decay referred to the time of the first PET acquisition, for each animal. The PET image reconstruction and analysis procedure is detailed in the Supporting Information section. ROIs were drawn over the abdominal aorta and the cava vein (for blood retention analysis), over the liver, spleen and kidneys. Organ and blood retention was calculated in units of %ID/g (see Supporting Information). The blood clearance half-lives were extracted by fitting the clearance curve with a sum of two exponentials, as follows:

$$y = A_0 + A \exp^{(-b*t)} + C*\exp^{(-d*t)} \qquad \text{Equation 2}$$

The area under the curve was measured to calculate the nanoparticle retention rate, expressed in units of (MBq/cc) × hour. To calibrate PET measurements, blood samples were extracted from the caudal vein at t = 60 minutes after the first injection, for each animal, and measured in a gamma counter (Auto-Gamma, Cobra II, Packard Instrument Company, Meriden, CT, USA) to determine the blood radioactivity concentration. Finally, 48 h after the injection of $Gd^{3+}/^{64}Cu^{2+}$-DTPA-M48SNs, mice were euthanized by intracardiac exsanguination. Organs of interest were extracted, weighed, and their activity was measured by gamma counter. Values were corrected for the radioactive decay, as well as for the gamma counter efficiency, and expressed in units of %ID and %ID/g of tissue.

Results and discussion

The MCM-48-type MSNs (with a 3D pore structure) were synthesized in basic media, followed by template extraction in ethanol.[33] As shown in Fig. 1 A-C, the particles are non-aggregated, well-defined and uniformly spherical (mean diameter by TEM: 150 nm). The reaction sequence that was used to graft DTPA, followed by chelation with Gd^{3+} and $^{64}Cu^{2+}$ ions, is schematically presented in Fig. 1 D-F. APTES was reacted with the silanol groups at the MSN surface (in toluene), to form "APTES-M48SNs", followed by grafting with DTPA ("DTPA-M48SN"). Finally, the particles are labeled with Gd^{3+} or $Gd^{3+}/^{64}Cu^{2+}$ ions in nanopure water (Fig. 1F).

Textural properties and TGA analysis. Porosity data, reported in Table 1. The final product (DTPA-M48SNs) had a surface area, pore volume and mesopore size of 847 m^2/g, 0.42 cm^3/g and 2.4 nm, respectively. Thermogravimetric analysis (TGA, Fig. S4) performed on APTES-M48SN and DTPA-M48SN, revealed a weight loss of 18.5% and 33.5%, respectively (15 % w/w attributed to DTPA in DTPA-M48SN), indicating the strong presence of DTPA in M48SNs.
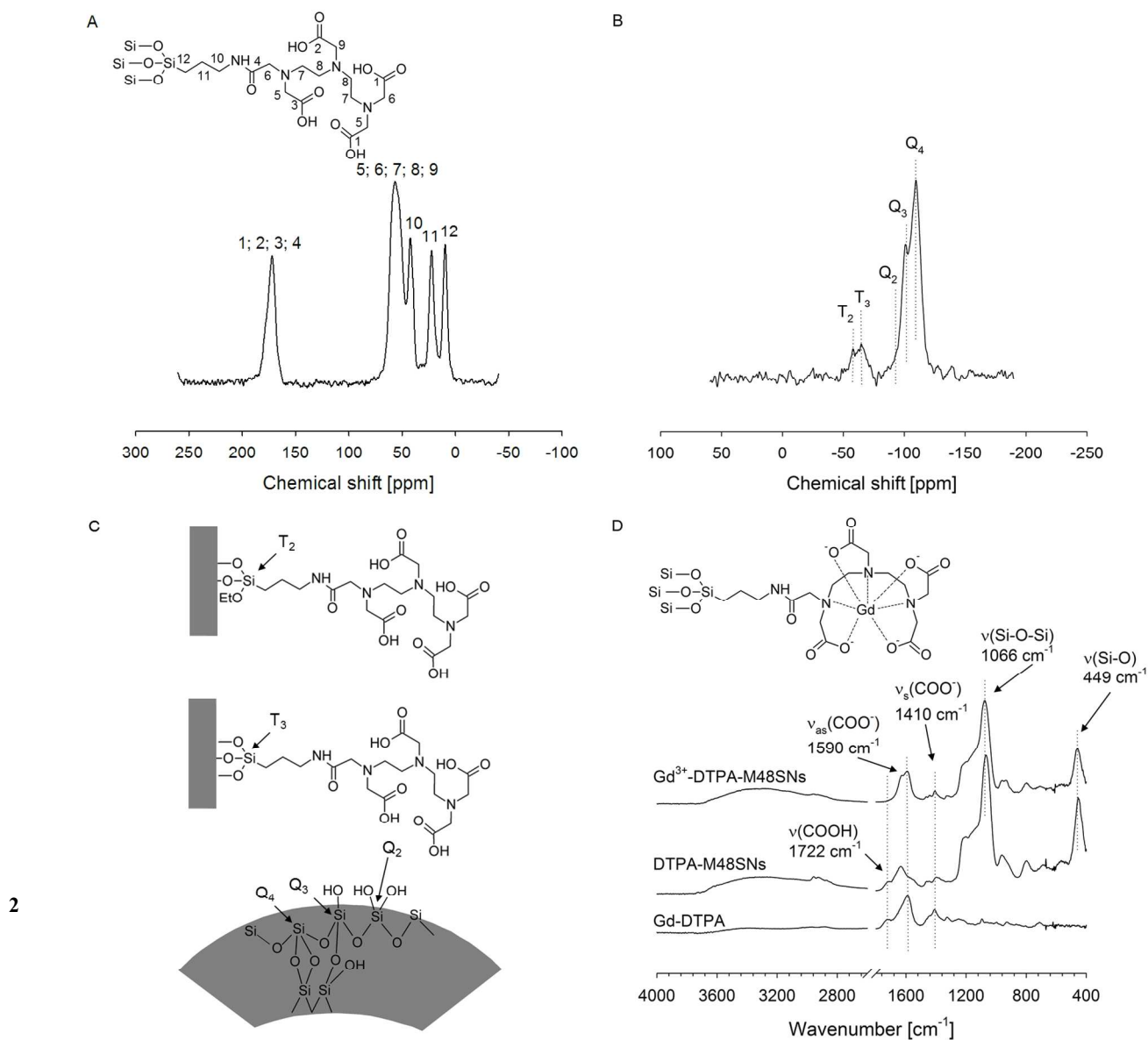
Physico-chemical characterisation (NMR, XPS, FTIR, EDX). The successful grafting of APTES and DTPA on M48SNs was further confirmed by NMR, XPS and FTIR spectroscopic characterization. First, NMR spectra of ^{13}C and ^{29}Si (Fig. 2A and 2B) confirmed the presence of APTES and the covalent reaction (on the ^{29}Si spectrum) of APTES with the silanol groups present at the surface of M48SNs. Indeed, the ^{13}C CP-MAS NMR spectrum of DTPA-M48SNs showed all the typical characteristic peaks of DTPA-APTES (ascribed in Fig. 2A). The ^{13}C peaks characteristics of DTPA were grouped into two major contributions: one group at – (160 – 180) ppm, corresponding to the five carbon atoms present in positions 1 - 4; one group at – (40 – 65) ppm, corresponding to the eight atoms present in positions 5 - 9. In addition, the ^{29}Si NMR spectrum (Fig. 2B) depicted a multicomponent peak in the -88 to -120 ppm range, which is associated with the Q_n groups of the silica framework (Q_n schematically represented in Fig. 2C). Furthermore, T_n groups from the silicon atoms contained by covalently-grafted silane molecules, were also evidenced (Fig. 2C) and confirmed the reaction of APTES on MSNs.[34]

FTIR spectra of Gd-DTPA, DTPA-M48SNs and Gd^{3+}-DTPA-M48SNs are presented in Fig. 2D. FTIR spectra confirmed the grafting of DTPA on M48SNs and the chelation of Gd^{3+}. First, the stretching bands of Gd^{3+}-DTPA-M48SNs matched the ones of Gd-DTPA and of DTPA-M48SNs. The observation of carboxylate bands in the FTIR spectra (Fig. 2D) confirmed the efficient chelation of Gd^{3+} by DTPA. Gd^{3+}-DTPA-M48SNs stretching bands are similar to the DTPA-M48SNs, except for the absorption band at 1722 cm^{-1}, which disappeared after the chelation of the Gd^{3+}. This indicates that all the carboxylic acids (COOH) in DTPA are deprotonated and used for the grafting on APTES-M48SNs or for the chelation of Gd^{3+}. The separation (Δ) between the symmetric and asymmetric bands of the carboxylate group indicates the coordination type. For the Gd^{3+}-DTPA-M48SNs, a wavenumber separation of 180 cm^{-1} was calculated, which corresponds to a bridging ligand.[35] As shown is Fig. 2D, the carboxylate separation is similar for Gd-DTPA and Gd^{3+}-DTPA-M48SNs, indicating that there is no modification of the chelation type between both products. The DTPA-M48SNs spectrum showed the DTPA stretches and also revealed the characteristic mesoporous silica nanoparticles bands.

Table 1 Textural properties of M48SNs and DTPA-functionalized M48SNs

Sample	Surface area [m^2/g]	Pore volume [cm^3/g]	NLDFT ads. Pore size [nm]
M48SNs	1633	1.34	3.6
DTPA-M48SNs	847	0.42	2.4

Physico-chemical characterization of M48SNs: (**A**) grafting of DTPA demonstrated by ^{13}C CP/NMR profile; (**B**) grafting of APTES on the silica network demonstrated by the ^{29}Si MAS NMR profile; (**C**) schematic representation of the Si-O bonds at the surface of M48SNs, as revealed by NMR; (**D**) FTIR profile of Gd-DTPA, DTPA-M48SNs and Gd^{3+}-DTPA-M48SNs.

Fig. 2

The XPS results clearly exhibited the presence of silicon, carbon, oxygen, nitrogen and gadolinium (Table 2). As expected, the characteristic silicon peak of mesoporous silica at 103.7 eV was observed for each nanoparticle system.[33] The grafting efficiency of APTES and DTPA was evidenced by the strong presence of C, N and O. For C the band at 285.0 eV (Table 2) is attributed to C-C and C-H; that at 286.5 eV to C-O and C-N; the one at 288.8 eV to C=O amide/acid. For N, the presence of

two components at binding energies of 399.8 eV and 402.0 eV were observed. The peak at 399.8 eV was attributed to amine (NH$_2$) groups and the contribution at 402.0 eV, to residual ammonium (NH$_3^+$) content from chemical extraction procedure. The presence of this contamination was observed for APTES-M48SNs (1.4%) and DTPA-M48SNs (0.8%) systems. The contributions of Si significantly decreased after the grafting procedures (Table 2). Consequently, an increase in the C/Si ratios

were observed, which confirmed that APTES and DTPA were　　　efficiently grafted on M48SNs.

Table 2 Surface composition of nanoparticles (from XPS survey spectra)

Sample	% C [285.0 eV:C-C/C-H] (286.5 eV:C-O/C-N) {288.8 eV:C=O amide/acid}	% O [532.8 eV:Si-O/COOH] (531.5 eV:Gd-OCO)	% N [399.8 eV:NH$_2$] (402.0 eV:NH$_3^+$)	% Si 103.7 eV:SiO	% Gd	C/Si
M48SNs	9.7	63.7 [63.7] (-)	-	26.6	-	0.37
APTES-M48SNs	25.8 [12.7] (13.1) {-}	47.0 [47.0] (-)	4.0 [2.6] (1.4)	21.6	-	1.19
DTPA-M48SNs	31.8 [13.5] (16.1) {2.2}	42.7 [42.7] (-)	6.9 [6.1] (0.8)	18.1	-	1.76
Gd^{3+}-DTPA-M48SNs	30.3 [14.2] (12.9) {3.2}	43.8 [36.2] (7.6)	6.5 [6.5] (-)	17.6	0.8	1.72

*The missing contribution to reach 100% of surface composition corresponds to the Cl contribution.

XPS further confirmed the chelation of Gd^{3+} by DTPA-M48SNs (0.8% of Gd), for a Gd/Si ratio of 0.045. This result indicates an efficient complexation of Gd^{3+} to DTPA-M48SNs, meaning suitable chelation conditions. Oxygen contribution revealed two peaks at binding energies of 532.8 eV and 531.5 eV. Peaks were assigned as follows: 532.8 eV to Si-O/COOH and 531.5 eV to Gd-OCO. The absence of a second silica peak at 102.1 eV indicates that there are no gadolinium silicate domains (Si-O-Gd).[33] Finally, because XPS is a surface technique, the Gd/Si ratio was also measured by EDX (on a HRTEM system). Gd/Si ratios of 0.064 at the outer surface of particles, and 0.058 at their core, confirmed that Gd was distributed not only at the outer surface of particles, but uniformly inside the mesopore structure. The chemical concentration of ^{64}Cu^{2+} was too low in ^{64}Cu^{2+}-DTPA-MSNs to reach detectability levels in XPS.

Colloidal stability and relaxometric properties. DLS revealed a hydrodynamic diameter size of 250 ± 76 nm, and a strong colloidal stability (Fig. 3A), confirmed by zeta potential (-20.6 mV at pH 7.5). Only a slight increase of hydrodynamic diameter was found after 6 months in 154 mM NaCl. The relaxometric potential of Gd^{3+}-DTPA-M48SNs was measured at clinical magnetic field strength (1.41 T, 60 MHz, 37 °C, Fig. 3B). The longitudinal relaxivity of Gd^{3+}-DTPA-M48SNs was r$_1$=17.6 mM^{-1}s^{-1} (r$_2$/r$_1$ ratio of 2.0), which is 5.3 times higher than for Gd-DTPA (see Table S1), and in the same order as for previous studies reported for Gd-MSNs (19.0 mM^{-1}s^{-1}, r$_2$/r$_1$ = 2.5; measured at 3T and room temperature).[30] The previous few relaxometric studies on Gd-labeled MSN were performed mainly with 2-D mesoporous networks, and they used different magnetic field strengths and temperature conditions. For some of them, precise relaxivity values were not reported.[26] For Gd^{3+}-DTPA-M48SNs, we measured r$_1$ and r$_2$ on a large range of magnetic field strengths (from 0.01 to 500 MHz for r$_1$ and 20 to 500 MHz for r$_2$, Fig. 3C). NMRD profiles revealed a relaxometric peak at 10 – 60 MHz, followed by a sharp decrease at fields >100 MHz, which is typical of NMRD profiles of nanoparticles and macromolecules labeled with paramagnetic chelates. For instance, Gd^{3+} chelates bound to human serum albumin, show a maximum peak at similar field strengths (~20 MHz).[36] This peak has been attributed to the fact that for nanoparticles and macromolecules, the rotational time of the compound is intrinsically higher than for free Gd^{3+} chelates. Finally, the presence of free Gd-DTPA would have been evidenced by strong dipolar dispersion at about 5 MHz.[37] Hence, the labeling of M48SNs with Gd^{3+} provides an efficient positive contrast enhancement effect at clinical magnetic field strengths (1 - 1.5 T; 40 - 60 MHz), which is moderate at higher fields (higher r$_2$/r$_1$ ratios). No evidence of sedimentation or aggregation was found either by DLS or in T$_1$-w. *in vitro* MRI images (Fig. S5).
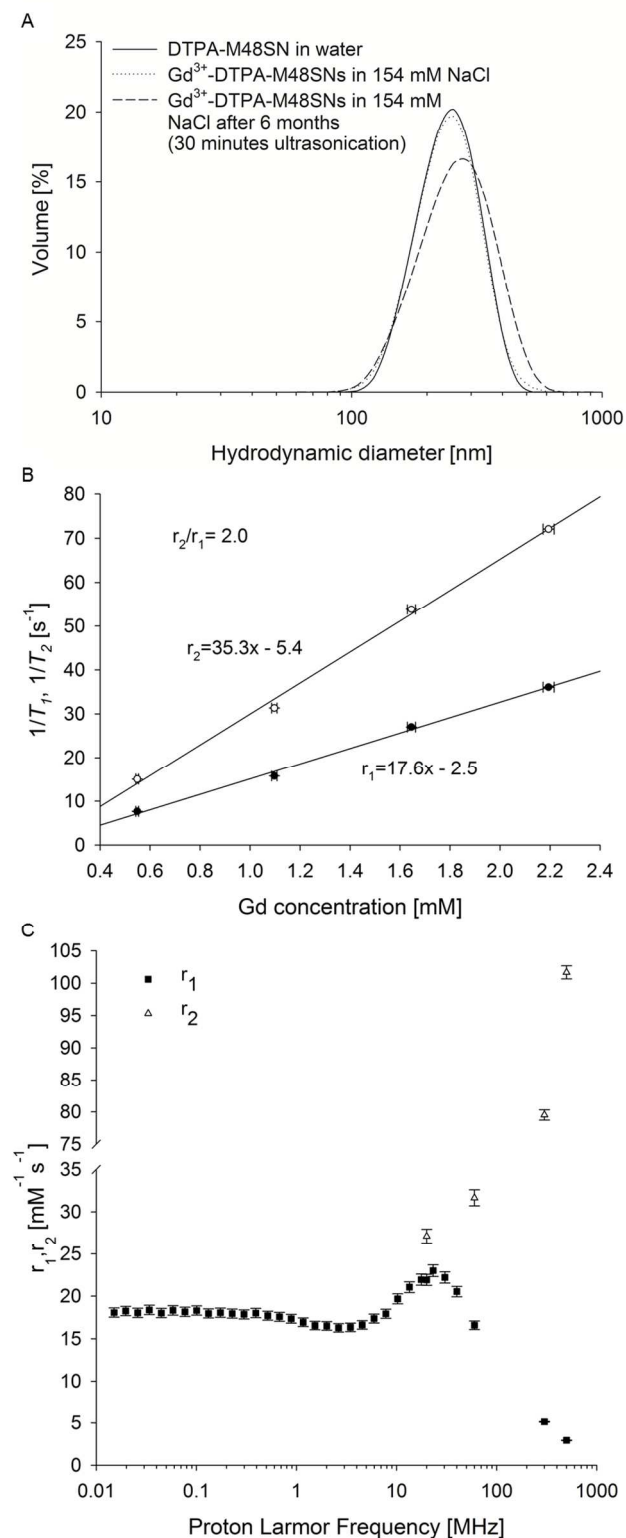
Fig. 3 DLS hydrodynamic diameter profiles and colloidal stability **(A)**. Contrast-enhancement potential of Gd^{3+}-DTPA-M48SN, relativities (r_1, r_2) measured at clinical magnetic field strength (1.41 T)**(B)**, and **(C)** NMRD profiles of Gd^{3+}-DTPA-M48SNs (r_1, r_2) at variable magnetic field strengths.

In vivo stability assessment

Gd^{3+}-DTPA-M48SNs were injected in mice (0.31 µmol Gd), and scanned in MRI for at least 1 hour (Fig. 4A). The injected dose was deliberately kept at a low level (12.4 µmol/kg or 0.31 µmol Gd/mouse for a 25-g animal), well below the potential cytotoxic thresholds of Gd-DTPA (typical clinical injections at 0.1 mmol/kg). A strong vascular signal enhancement was evidenced and quantified in the first minutes following the injection, corroborating the high relaxivities measured for Gd^{3+}-DTPA-M48SNs, stronger than for free Gd^{3+}-DTPA. The signal enhancement was monitored on the abdominal aorta (empty arrow in Fig. 4A), confirming the significant concentration of Gd in the blood (Fig. S6A), as well as the retention of a signal enhancement effect up to 90 minutes after the injection. The signal in the liver remained relatively stable over time (Fig. S6B), whereas a moderate and progressive signal enhancement was noted in the bladder (Fig. S6C), indicating the leaching of a very limited fraction of Gd^{3+}-DTPA from the M48SNs. No evidence of signal enhancement was noted in the kidneys. This is a significant finding because, on such high specific surface systems, the presence of DTPA chelators only adsorbed (and not covalently bound) to the main nanoparticle framework, could lead to excessive leaching of Gd^{3+}-DTPA in the blood, in the first seconds following injection of the compound. The absence of signal enhancement in the kidneys confirms that Gd^{3+}-DTPA attached using the chemical procedure described in the experimental section, does not leach from the nanoparticles upon injection.

After MRI studies, the distribution of Gd^{3+}/$^{64}Cu^{2+}$-DTPA-M48SNs was monitored by PET (Fig. 4B). The activity of the suspension was 4.49 mCi after the purification, with a $^{64}Cu^{2+}$ chelation yield of 54%. Dynamic and static PET scans performed over 48 hours, revealed a strong accumulation of particles in the liver and in the spleen and, more importantly, in the gastro-intestinal system (Fig. 4B). Gastrointestinal excretion was evidenced at 24 h and 48 h, and confirmed by biodistribution data at 48 h (Table 3). In spite of a very careful examination of the PET images in the first seconds following injections, then at every acquisition time, no evidence of signal accumulation was found in the kidney area. A moderate to high kidney activity would have indicated the presence of detached ^{64}Cu-DTPA from the MSN structures. In fact, i.v.-injected ^{64}Cu is expected to be eliminated through the kidneys within 2 h post injection.[38] The presence of free ^{64}Cu would also have been clearly indicated by activities in the bladder and the kidneys, in the first hour following the injection.

The dynamic PET and MRI scans were then used to plot the blood clearance (Fig. 5A and S6A). In the dynamic PET acquisitions, regions of interest (ROI) of the abdominal aorta and the cava vein were plotted and converted in %ID/g of blood. Blood clearance half-lives were calculated on the results of four (4) animals, and fitted according to a model of two (2) exponential curves (fast-decaying component: mean $t_{1/2\ blood}$ = 4.5 min ± 2.4; slow-decaying component: $t_{1/2\ blood}$ = 137 min ± 11, respectively). Finally, Fig. 5B depicts the evolution of % ID/g of tissue as a function of time for ROIs integrated on the liver and spleen areas. The results were corrected for ^{64}Cu physical decay. The left part of the graph corresponds to the 60-min dynamic acquisition data, whereas the right part corresponds to the static acquisitions at 6, 12, 24 and 48 h post-injection. In the liver, a maximum peak (~88% ID/g) was reached in the first minute after injection, followed by a rapid decrease to ~42% ID/g. This initial peak corresponds to the nanoparticles present in the vascular system just after injection. After this first initial peak, the liver signal progressively increased, then

plateaued (~65% ID/g). A strong activity decrease was noted within the first 48 hour after injection. Similar profiles were revealed for the spleen, with activity concentrations about half of those calculated in the liver (~27% ID/g) few minutes after the injection. The biological half-lives of the nanoparticles in the liver and in the spleen were measured in the 6 – 48 h period, and correspond to 14.8 h and 12.9 h, respectively (Fig. 5B). Finally, the comprehensive *ex vivo* biodistribution study performed at 48 h (Table 3), revealed that $Gd^{3+}/^{64}Cu^{2+}$-DTPA-M48SNs were mainly found in the liver (~30.1% ID), which is consistent with PET results. A high level of activity was found in the intestine (~18.1% ID). A moderate activity level was found in the blood (4.94% ID), as well as in the heart (~1.09% ID) and in the lungs (~1.65% ID).

Understanding the retention to organs, elimination, and early signs of degradation of the particles *in vivo*, is a priority in the perspective of transferring MSN-based technologies into approved clinical procedures. One of the most fundamental steps, is to demonstrate that metal chelates attached on nanoparticles that have such high specific surface values as MSNs, remain strongly attached once submitted to *in vivo* conditions. The absence of signal in the kidneys in the bladder, confirms the strong attachment of metal chelates at the surface of the particles. Then, the blood clearance of MSNs as well as uptake in organs such as liver, spleen and kidneys are expected to occur within minutes following i.v. injection. Therefore, efficient, quantitative and time-resolved imaging modalities must be used to reveal the dynamics of such processes. Dual MRI/PET acquisition protocols provide a straightforward and systematic methodology allowing the precise *in vivo* quantification of nanoparticle blood retention (by MRI), excretion by the kidneys through the urine (by MRI), as well as dynamic measurement of liver, spleen, lung, and kidney uptake and clearance (by PET).

In the present study, the uptake to critical organs such as liver (30.1%), spleen (0.72%) and lungs (1.65%) at 48 h, was similar to data previously found for MSN showing zeta potential -20.5 mV, and measured at 72 h after injection (MSNP-PEG).[39] $Gd^{3+}/^{64}Cu^{2+}$-labeled MSNs were found mainly in the liver and in the spleen within a few minutes after injection (Fig. 5C). After the high-intensity peak initially detected in the liver, and corresponding to the initial vascular influx of radioactive MSNs, a progressive uptake of MSNs occurs at the same rate in the liver and in the spleen. After 7

minutes, the uptake of the particles in the liver and in the spleen reaches a plateau, followed by progressive elimination. This is the first time a quantitative and dynamic measurement of liver and spleen MSN uptake, retention, and elimination, is performed in real time. MSNs appear to be strongly eliminated from the liver and from the spleen. Interactions with proteins, serum components and immune cells in the blood may affect the behavior of template-extracted MSNs and initiate their degradation.[40-42] Calcined nanoparticles, on the other hand, are more resistant to degradation when submitted to physiological media.[43] It is generally assumed that biocompatible nanoparticles which remain in the body for a few hours, delivering a treatment, followed by a strong elimination through the urinary or gastrointestinal tracts, would attenuate the toxicity risks and moderate their potential long-term retention in organs.

The precision of dynamic PET studies performed here provided new valuable insights into blood clearance data (Fig. 5A). Two (2) different regimes were identified: first, a more rapid mechanism of elimination seems to occur (mean $t_{1/2\ blood}$ = 4.5 min ± 2.4), then, as second, slower contribution, is noticed ($t_{1/2\ blood}$ = 137 min ± 11). The first contribution is most probably due to the larger fraction of particles that are rapidly sequestered by the macrophages, followed by their entrapment in the liver and spleen. The slower contribution is attributed to larger particles (>200 nm) possibly delayed in the fine vasculature of several organs such as in the liver, and in the lungs. Overall, the presence of two clear components in the blood clearance profiles of MSNs is a significant observation that would deserve further investigation

Finally, the *ex vivo* biodistribution study performed at 48h, revealed a strong presence of particles in the intestine (18.1% ID at 48 h; Fig. 4B), confirming that the major route for the degradation of DTPA-labeled MSNs is through the gastrointestinal tract. Significant contributions were also found in the kidneys (2.27%) but relatively weak ones in the bladder (0.06%). The retention of vascular radioactivity at 48h (4.94% ID), suggests the occurrence of a vascular uptake of small fragments of MSNs, possibly at the intestinal level. The exact mechanism of this phenomenon should be studied in detail in order to comprehensively understand the pharmacokinetics and clearance mechanisms of silica nanoparticles.
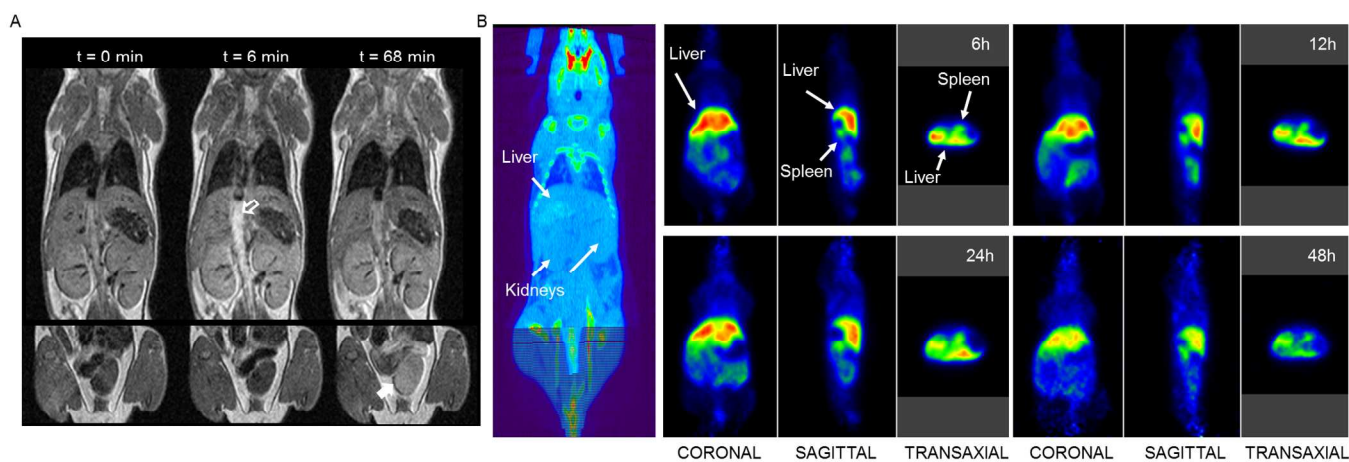

Fig. 4 MRI images of mice injected i.v. with Gd^{3+}-DTPA-M48SNs (**A**). Empty arrow: vascular signal-enhancement effect after injection of the particles. PET images of mice injected with $Gd^{3+}/^{64}Cu^{2+}$-DTPA-M48SNs (**B**). Left: coronal "scout" CT map to localize liver and kidneys. Right: series of coronal, sagittal and axial PET images acquired at time points. No evidence of radioactive uptake or clearance was found in the kidneys.
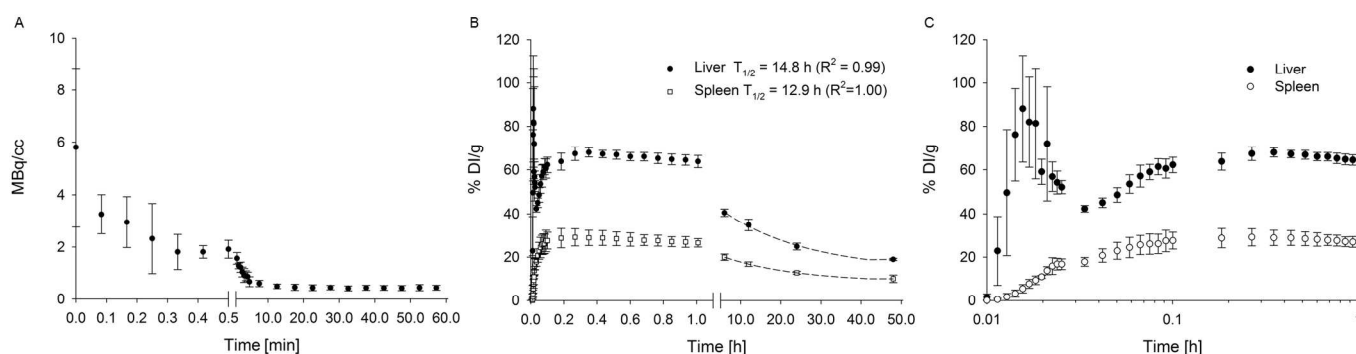
Fig. 5 Dynamic blood clearance profiles measured by PET (**A**); uptake and retention of M48SNs in the liver and in the spleen (**B-C**).

Table 3 Biodistribution of $Gd^{3+}/^{64}Cu^{2+}$-DTPA-M48SNs after 48 hours (n = 4). Total injected activity (ID) is based on the average of 3 standards

Organ	48 hours			
	% ID	±	% ID/g	±
Blood	4.94	0.76	4.66	0.72
Liver	30.1	1.8	30.3	2.0
Spleen	0.72	0.13	9.3	1.3
Kidney	2.27	0.03	17.08	0.85
Lungs	1.65	0.10	12.9	1.3
Pancreas	1.14	0.16	4.86	0.36
Heart	1.09	0.07	11.96	0.44
Intestine	18.1	1.0	12.27	0.47
Stomach	1.53	0.17	8.80	0.71
Bladder	0.06	0.00	3.31	0.48

Conclusions

The strong attachment of metal chelates at the surface of 3-D nanostructured mesoporous silica nanoparticles, was characterised by FTIR, XPS, and NMR. The particles demonstrated a very strong colloidal stability *in vitro*. The relaxometric study performed with Gd^{3+}-DTPA-M48SNs revealed a high contrast enhancement potential in MRI, as well as a signature typical of paramagnetic nanoparticles. $Gd^{3+}/^{64}Cu^{2+}$-DTPA-M48SNs were injected in mice, and visualized in MRI and in PET. No significant activity was detectable in the bladder with PET, whereas a slight signal increase was measured with MRI, but only at 90 min. post-injection. This confirms the very limited detachment of DTPA from the M48SN cores with the chelat grafting methodology used in this study. PET and biodistribution data confirmed that MSN excretion occurs massively by the gastrointestinal route following their uptake by the hepatic system. No evidence was found that the transit of MSN *in vivo*, leads to DTPA detachment and elimination in the urine. This demonstrates the quality and strength of DTPA anchoring at the silica surfaces, and validates this approach for further development in the field of PET/MRI-assisted drug delivery procedures using MSNs.

Acknowledgements

Notes and references

[a] Centre de recherche du Centre hospitalier universitaire de Québec (CR-CHUQ), axe Médecine Régénératrice, Québec, G1L 3L5, QC, Canada

Phone: 1-418-525-4444 ext: 52366; Fax: 1-418-525-4372; E-mail: marc-andre.fortin@gmn.ulaval.ca

[b] Department of Mining, Metallurgy and Materials Engineering, Université Laval, Québec, G1V 0A6, QC, Canada

[c] Department of Chemistry, Université Laval, Québec, G1V 0A6, QC, Canada

Phone: 1-418-656-7812; Fax: 1-418-656-7916;

E-mail: freddy.kleitz@chm.ulaval.ca

d Centre de recherche sur les matériaux avancés (CERMA), Université Laval, Québec, G1V 0A6, QC, Canada

e Sherbrooke Molecular Imaging Center, CRCHUS, and Department of Nuclear Medicine and Radiobiology, Université de Sherbrooke, Sherbrooke, J1H 5N4, QC, Canada

f Service de physique biomédicale, Université de Mons, Mons, B7000, Belgium

* Corresponding authors

1. J. M. Rosenholm, V. Mamaeva, C. Sahlgren and M. Linden, *Nanomedicine*, 2012, **7**, 111-120.
2. Q. J. He and J. L. Shi, *J Mater Chem*, 2011, **21**, 5845-5855.
3. R. Wittig, J. M. Rosenholm, E. von Haartman, J. Hemming, F. Genze, L. Bergman, T. Simmet, M. Linden and C. Sahlgren, *Nanomedicine (Lond)*, 2013.
4. J. M. Rosenholm, C. Sahlgren and M. Linden, *Nanoscale*, 2010, **2**, 1870-1883.
5. V. Mamaeva, C. Sahlgren and M. Linden, *Adv Drug Deliv Rev*, 2013, **65**, 689-702.
6. J. E. Lee, D. J. Lee, N. Lee, B. H. Kim, S. H. Choi and T. Hyeon, *J Mater Chem*, 2011, **21**, 16869-16872.
7. J. L. Vivero-Escoto, R. C. Huxford-Phillips and W. B. Lin, *Chem Soc Rev*, 2012, **41**, 2673-2685.
8. J. Lu, Z. X. Li, J. I. Zink and F. Tamanoi, *Nanomed-Nanotechnol*, 2012, **8**, 212-220.
9. J. L. Gu, S. S. Su, M. J. Zhu, Y. S. Li, W. R. Zhao, Y. R. Duan and J. L. Shi, *Microporous and Mesoporous Materials*, 2012, **161**, 160-167.
10. Y. Chen, H. R. Chen, S. J. Zhang, F. Chen, S. K. Sun, Q. J. He, M. Ma, X. Wang, H. X. Wu, L. X. Zhang, L. L. Zhang and J. L. Shi, *Biomaterials*, 2012, **33**, 2388-2398.
11. J. Lu, M. Liong, Z. X. Li, J. I. Zink and F. Tamanoi, *Small*, 2010, **6**, 1794-1805.
12. T. Asefa and Z. M. Tao, *Chem Res Toxicol*, 2012, **25**, 2265-2284.
13. X. L. Huang, L. L. Li, T. L. Liu, N. J. Hao, H. Y. Liu, D. Chen and F. Q. Tang, *Acs Nano*, 2011, **5**, 5390-5399.
14. T. L. Liu, L. L. Li, X. Teng, X. L. Huang, H. Y. Liu, D. Chen, J. Ren, J. Q. He and F. Q. Tang, *Biomaterials*, 2011, **32**, 1657-1668.
15. K. C. W. Wu and Y. Yamauchi, *J Mater Chem*, 2012, **22**, 1251-1256.
16. Q. He, J. Shi, F. Chen, M. Zhu and L. Zhang, *Biomaterials*, 2010, **31**, 3335-3346.
17. Slowing, II, J. L. Vivero-Escoto, C. W. Wu and V. S. Lin, *Adv Drug Deliv Rev*, 2008, **60**, 1278-1288.
18. M. Liong, J. Lu, M. Kovochich, T. Xia, S. G. Ruehm, A. E. Nel, F. Tamanoi and J. I. Zink, *ACS Nano*, 2008, **2**, 889-896.
19. J. L. Vivero-Escoto, Slowing, II, B. G. Trewyn and V. S. Lin, *Small*, 2010, **6**, 1952-1967.
20. B. G. Trewyn, Slowing, II, S. Giri, H. T. Chen and V. S. Lin, *Acc Chem Res*, 2007, **40**, 846-853.
21. I. I. Slowing, B. G. Trewyn, S. Giri and V. S. Y. Lin, *Advanced Functional Materials*, 2007, **17**, 1225-1236.
22. P. P. Yang, S. L. Gai and J. Lin, *Chem Soc Rev*, 2012, **41**, 3679-3698.
23. A. E. Garcia-Bennett, *Nanomedicine-Uk*, 2011, **6**, 867-877.
24. J. M. Rosenholm, C. Sahlgren and M. Linden, *Current drug targets*, 2011, **12**, 1166-1186.
25. M. Benezra, O. Penate-Medina, P. B. Zanzonico, D. Schaer, H. Ow, A. Burns, E. DeStanchina, V. Longo, E. Herz, S. Iyer, J. Wolchok, S. M. Larson, U. Wiesner and M. S. Bradbury, *Journal of Clinical Investigation*, 2011, **121**, 2768-2780.
26. X. L. Huang, F. Zhang, S. Lee, M. Swierczewska, D. O. Kiesewetter, L. X. Lang, G. F. Zhang, L. Zhu, H. K. Gao, H. S. Choi, G. Niu and X. Y. Chen, *Biomaterials*, 2012, **33**, 4370-4378.
27. F. Carniato, L. Tei, M. Cossi, L. Marchese and M. Botta, *Chem-Eur J*, 2010, **16**, 10727-10734.
28. F. Carniato, L. Tei, W. Dastru, L. Marchese and M. Botta, *Chemical Communications*, 2009, 1246-1248.
29. K. M. L. Taylor, J. S. Kim, W. J. Rieter, H. An, W. L. Lin and W. B. Lin, *Journal of the American Chemical Society*, 2008, **130**, 2154-+.
30. J. L. Vivero-Escoto, K. M. Taylor-Pashow, R. C. Huxford, J. Della Rocca, C. Okoruwa, H. An and W. Lin, *Small*, 2011, **7**, 3519-3528.
31. T. W. Kim, P. W. Chung, Slowing, II, M. Tsunoda, E. S. Yeung and V. S. Lin, *Nano letters*, 2008, **8**, 3724-3727.
32. M. Bergeron, J. Cadorette, M.-A. Tétrault, J.-F. Beaudoin, J.-D. Leroux, R. Fontaine and R. Lecomte, *Physics in Medicine and Biology*, 2014, **59**, 661-678.
33. R. Guillet-Nicolas, J.-L. Bridot, Y. Seo, M.-A. Fortin and F. Kleitz, *Advanced Functional Materials*, 2011, **21**, 4653-4662.
34. J. Kobler, K. Moller and T. Bein, *Acs Nano*, 2008, **2**, 791-799.
35. F. Soderlind, H. Pedersen, R. M. Petoral, P. O. Kall and K. Uvdal, *J Colloid Interf Sci*, 2005, **288**, 140-148.
36. L. V. Elst, F. Maton, S. Laurent, F. Seghi, F. Chapelle and R. N. Muller, *Magnetic Resonance in Medicine*, 1997, **38**, 604-614.
37. É. Toth, L. Helm and A. E. Merbach, in *Contrast Agents I*, Topics in Current Chemistry, 2002, pp. 61-101.
38. M. L. Schipper, Z. Cheng, S. W. Lee, L. A. Bentolila, G. Iyer, J. H. Rao, X. Y. Chen, A. M. Wul, S. Weiss and S. S. Gambhirl, *Journal of Nuclear Medicine*, 2007, **48**, 1511-1518.
39. H. Meng, M. Xue, T. Xia, Z. Ji, D. Y. Tarn, J. I. Zink and A. E. Nel, *ACS Nano*, 2011, **5**, 4131-4144.
40. M. P. Monopoli, D. Walczyk, A. Campbell, G. Elia, I. Lynch, F. B. Bombelli and K. A. Dawson, *J Am Chem Soc*, 2011, **133**, 2525-2534.
41. T. Cedervall, I. Lynch, S. Lindman, T. Berggard, E. Thulin, H. Nilsson, K. A. Dawson and S. Linse, *Proceedings of the National Academy of Sciences of the United States of America*, 2007, **104**, 2050-2055.
42. M. Lundqvist, J. Stigler, G. Elia, I. Lynch, T. Cedervall and K. A. Dawson, *Proceedings of the National Academy of Sciences of the United States of America*, 2008, **105**, 14265-14270.
43. Q. He, J. Shi, M. Zhu, Y. Chen and F. Chen, *Micropor Mesopor Mat*, 2010, **131**, 314-320.
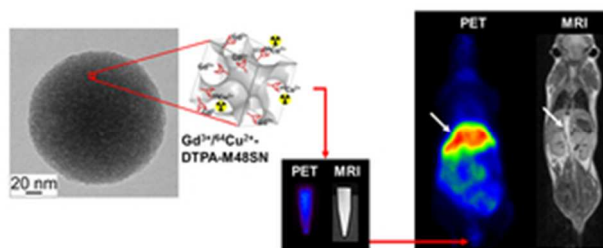
The physico-chemical characterization and dual in vivo imaging (PET/MRI) of MSNs functionalized with DTPA and labeled with Gd3+ and 64Cu2+.
26x10mm (300 x 300 DPI)